Numerical Prediction of Roll Damping and Magnus Dynamic Derivatives for Finned Projectiles at Angle of Attack

Vishal A. Bhagwandin[1]
U.S. Army Research Laboratory, Aberdeen Proving Ground, MD 21005

The roll damping and Magnus dynamic derivatives, as well as total aerodynamic coefficients, were numerically predicted for two basic fin-stabilized projectiles at a supersonic Mach number of 2.49 for angles of attack ranging from -5 to 90 degrees. The aerodynamic coefficients were computed via time-accurate Reynolds-averaged Navier Stokes numerical methods, and were compared with archival wind tunnel data. Fair to excellent comparisons with experiment were obtained for the total and dynamic coefficients for the full angle of attack range, except for axial force which was overpredicted. Numerical modeling parameter studies were conducted to include dependence on spin rate, grid resolution, temporal resolution and other numerical convergence parameters.

Nomenclature & Abbreviations

C_X	= axial force coefficient
C_Y	= side force coefficient
C_N	= normal force coefficient
C_l	= roll moment coefficient
C_m	= pitch moment coefficient
C_n	= yaw moment coefficient
C_{l_p}	= roll damping moment coefficient
C_{Y_p}	= Magnus force spin derivative coefficient
C_{n_p}	= Magnus moment spin derivative coefficient
$C_{Y_{p\alpha}}$	= Magnus force derivative coefficient
$C_{n_{p\alpha}}$	= Magnus moment derivative coefficient
α	= pitch plane angle of attack, degrees or radians
p	= spin rate/roll rate, rad/s
Ω, p'	= non-dimensional roll rate = $pD/2V$
$\emptyset$	= roll angle, degrees or radians
f	= roll frequency, Hz
t	= time, s
Δt	= transient physical/global timestep, s
N	= global iterations per rotation cycle
M	= freestream Mach number
V	= freestream velocity, m/s
D	= projectile base diameter = 1 caliber, m
S	= reference surface area = $\pi D^2/4$, m^2
ρ	= freestream density, kg/m^3

---

[1] Aerospace Engineer, WMRD Flight Sciences Branch, vishal.a.bhagwandin.civ@mail.mil. AIAA Member.

American Institute of Aeronautics and Astronautics

P_0	= total pressure, Pa
T_0	= total temperature, K
Re_d	= Reynolds number, based on projectile diameter
k	= turbulent kinetic energy, m^2/s^2
ε	= turbulent dissipation rate, m^2/s^3
y^+	= non-dimensional wall distance
aoa	= angle of attack
rad	= radians
ANF	= Army-Navy Basic Finner
AFF	= Air Force Modified Basic Finner
CFD	= computational fluid dynamics
RANS	= Reynolds-averaged Navier-Stokes

I. Introduction

ACCURATE prediction of dynamic stability derivatives is critical to the successful design and analysis of projectile munitions within the Army and other DoD agencies. As a complement to free-flight experiments, wind tunnel testing, and analytical estimation, computational fluid dynamics (CFD) is utilized as an efficient and cost-effective design tool for numerically predicting the in-flight aerodynamic forces, moments and stability derivatives of a projectile. Stability derivatives are a measure of how the aerodynamic forces and moments change in response to changes in flight states (such as angle of attack, velocity, spin etc.). Current advances in the maneuverability of projectiles necessitate accurate dynamic stability predictions at high angles of attack. Most experimental[1-6] and numerical[7-22] studies have successfully demonstrated the ability to obtain the dynamic stability derivatives at zero angle of attack for a range of projectiles and flight conditions. This study seeks to extend current advanced numerical techniques to predict dynamic stability derivatives, in particular the roll damping and Magnus derivatives, at angles of attack up to 90° for fin-stabilized projectiles.

To numerically compute the dynamic derivatives at a given angle of attack and Mach number, a rolling motion is simulated at a constant spin rate about the body-fixed x-axis of the projectile. The resulting time dependent flowfield is computed by the solving the three-dimensional, compressible, unsteady Reynolds-Averaged Navier-Stokes (RANS) fluid dynamics equations. The flow solution is then analyzed using simple flight mechanics theory to calculate the dynamic derivatives. The complex aerodynamic interactions at high angles of attack, such as vortex-body interactions, shock-body interactions and low-speed wake flows, combined with the forced spinning motion, presents a challenge to accurately predict the dynamic derivatives due to the non-linear unsteady behavior of the aerodynamic forces and moments acting on the projectile.

Two fin-stabilized projectile test models were used for the simulations, viz, the Army-Navy Basic Finner Missile (ANF) and the Air Force Modified Basic Finner Missile (AFF). These projectiles have been used as reference projectiles for many years and have been extensively tested in aeroballistic free-flight ranges and wind tunnels.[1-6] Archival experimental data was obtained from wind tunnel tests performed by Arnold Engineering and Development Center (AEDC) at Arnold Air Force Base, Tennessee.[1] Data was available for Mach numbers in the range 0.22–2.5, angles of attack in the range -5–90°, and Reynolds number, based on projectile diameter, in the range 1.05–5.97×10^5. This paper presents numerical results for both the ANF and AFF with zero fin cant, at a single Mach number of 2.49 and angles of attack ranging from -5–90°.

II. Background

All forces and moments are measured with respect to the projectile-fixed coordinate system whose x-axis is positive in the 'nose-to-tail' direction, z-axis is positive 'up' and whose origin is at the center of gravity of the projectile. Also note that the projectiles are symmetric about the x-z and x-y planes without beveled or canted fins.

Rolling, for the purpose of this study, is the motion whereby the projectile flies at a constant pitch angle, α, with respect to the freestream velocity vector while undergoing a constant angular rotation, p, about its body-fixed x-axis. During this motion the projectile experiences a roll damping moment that serves to oppose the spin of the projectile. Thus, for positive roll, the roll damping moment should be negative to enable dynamically stable flight. Eq. (1)[23-25] defines the scalar magnitude of the roll damping moment. The roll damping moment is proportional to the spin rate, p. It is common practice in exterior ballistics to non-dimensionalize the spin rate as $\Omega = pD/2V$. This non-

dimensional spin rate can be interpreted as the spin per caliber of travel, or as the ratio of axial spin to forward velocity.[24] C_{l_p} is the roll damping moment spin derivative coefficient, defined by Eq. (4).

The Magnus force and moment result from unequal fluid pressures on opposite sides of the projectile body due to viscous interactions between the fluid and spinning surface. The Magnus force is defined by Eq. (2),[23-25] and usually small at low angles of attack. It is positive for negative spin rates and positive angles of attack in the aforementioned coordinate system. The Magnus moment, defined by Eq. (3),[23-25] can be positive or negative depending on projectile geometry, center of gravity location, angle of attack and Mach number. Typically, the Magnus moment can have a significant impact on the dynamic stability of the projectile. Both the Magnus force and Magnus moment are proportional to the product of the spin rate and the sine of the total angle of attack. Since in this study yawing motions are not considered, the total angle of attack is just the pitch angle of attack, α. Due to the non-linear variation of the Magnus force and moment with angle of attack, the experiment only computes the spin derivative coefficients C_{Y_p} and C_{n_p}, defined in Eqs. (5) and (6), instead of the traditional derivative coefficients, $C_{Y_{p\alpha}}$ and $C_{n_{p\alpha}}$.

$$\text{Roll Damping Moment} = \frac{1}{2}\rho V^2 SD \left(\frac{pD}{2V}\right) C_{l_p} \tag{1}$$

$$\text{Magnus Force} = \frac{1}{2}\rho V^2 S \left(\frac{pD}{2V}\right) C_{Y_{p\alpha}} \sin\alpha \tag{2}$$

$$\text{Magnus Moment} = \frac{1}{2}\rho V^2 S \left(\frac{pD}{2V}\right) C_{n_{p\alpha}} \sin\alpha \tag{3}$$

$$C_{l_p} = \frac{\partial C_{l_t}}{\partial\Omega} \text{ rad}^{-1} \tag{4}$$

$$C_{Y_p} = \frac{\partial C_Y}{\partial\Omega} \text{ rad}^{-1} \tag{5}$$

$$C_{n_p} = \frac{\partial C_n}{\partial\Omega} \text{ rad}^{-1} \tag{6}$$

$$\Omega = \frac{pD}{2V} \text{ rad} \tag{7}$$

For the simulations, the non-dimensional spin rate, Ω, is judiciously chosen and the spin rate, p, is calculated via Eq. (7) for a given Mach number. Several non-dimensional spin rates were tested, viz. Ω=0.00389, 0.015 and 0.025 to verify the relationship between the total coefficients (C_{l_t}, C_Y and C_n) and spin rate. Note that for the remainder of this paper, unless otherwise stated, the terms 'spin rate' and 'non-dimensional spin rate' are used interchangeably. Since the simulations also require specification of the spin frequency, f, and timestep, Δt, these are calculated via,

$$f = \frac{p}{2\pi} = \frac{V\Omega}{\pi D} \tag{8}$$

$$\Delta t = \frac{1}{Nf} = \frac{\pi D}{NV\Omega} \tag{9}$$

where N is the chosen number of numerical iterations per rotation.

III. Geometry and Computational Methodology

A. Projectile Configurations and Experimental Test Data

The Army-Navy Basic Finner (ANF) and the Air Force Modified Basic Finner (AFF) projectiles were used as test models. Figure 1 shows the geometry details of both projectiles. Both projectiles had a diameter of 31.75 mm and consisted of a 2.836-caliber nose followed by a 7.164-caliber cylindrical body and four symmetrically positioned fins. The ANF consisted of a 10° conical nose, while the AFF consisted of a tangent ogive nose. The ANF's fins measured 1x1-caliber, with a sharp leading edges, and thicknesses of 0.08 calibers at the trailing edge. The AFF's fins were a clipped-delta shape with sharp leading and trailing edges. The fins for both projectiles were uncanted for this study. Fin dimensions are also shown in Figure 1. The centers of gravity of the ANF and AFF were located 6.1 and 5.0 calibers, respectively, from the nose tip. Their axial moments of inertia were 0.001329 kg-m[2] and 0.001220 kg-m[2], respectively.

For comparison with CFD results, experimental data was obtained from 1976 experiments performed by Arnold Engineering and Development Center (AEDC) at Arnold Air Force Base, Tennessee[1] in their von Karman Supersonic Wind Tunnel. The finner models were mounted at a fixed angle of attack via the apparatus shown in Figure 2, and were spun up to a desired spin rate. The models were then allowed to freely despin while roll position, time, forces and moments were recorded. The dynamic derivative coefficients (C_{l_p}, C_{Y_p}, C_{n_p}) were then computed using standard reduction procedures and curve fitting techniques across multiple data sets. Additionally, total axial force coefficient (C_X), total longitudinal coefficients (C_N and C_m), and total directional coefficients (C_Y and C_n) were obtained at a spin rate of $p{\approx}100$ rad/s or $\Omega{\approx}0.00389$. Reference 1 provides details of the test procedures and data acquisition. Experimental data used in this study were for the wind tunnel conditions listed in Table 1.
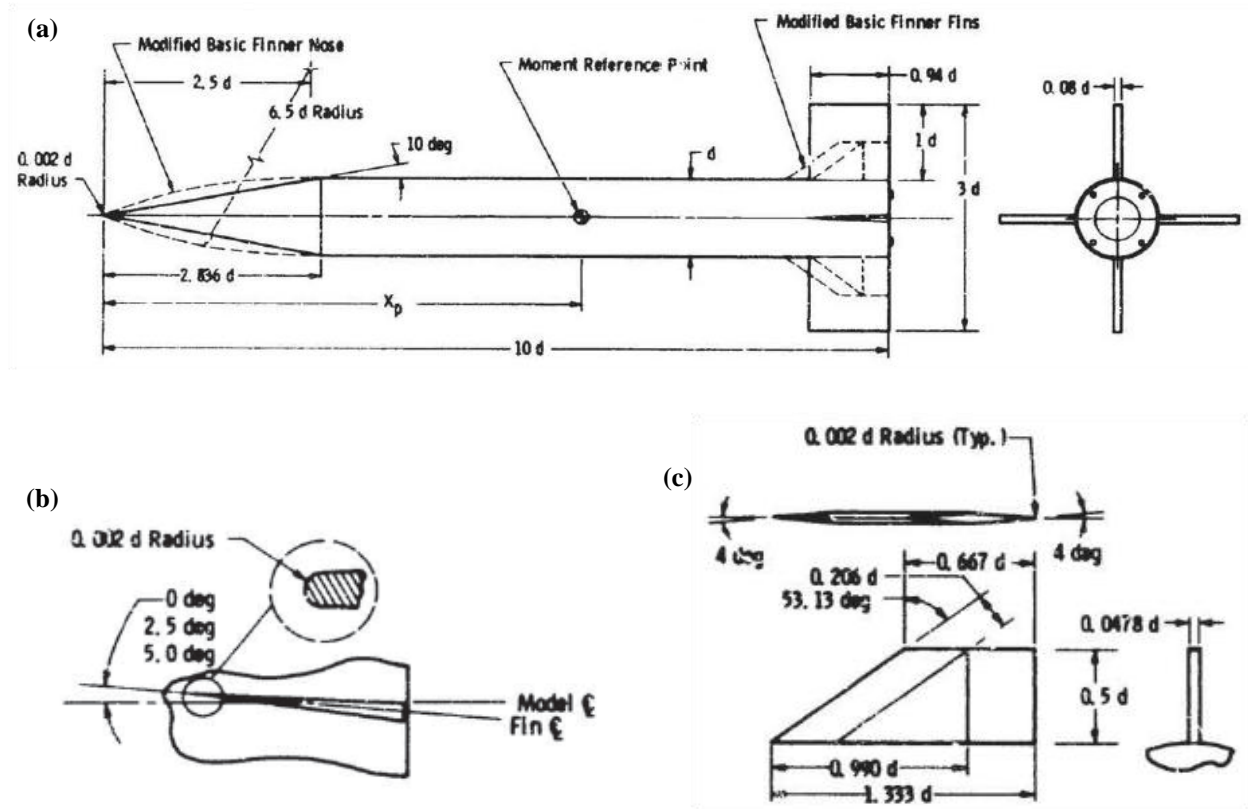

Figure 1. ANF and AFF model dimensions, d=31.75 mm: (a) ANF and AFF, (b) ANF fin detail, and (c) AFF fin detail [AEDC-TR-76-58, Ref. 1].
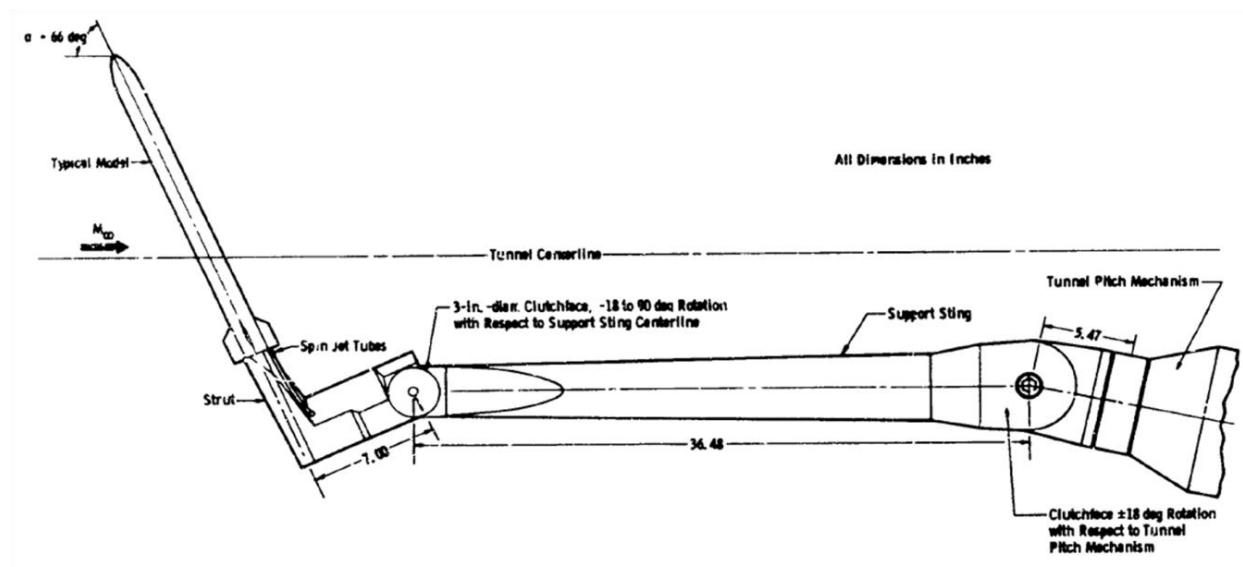
Figure 2. AEDC wind tunnel test apparatus [AEDC-TR-76-58, Ref. 1].

Table 1. AEDC Wind Tunnel Conditions

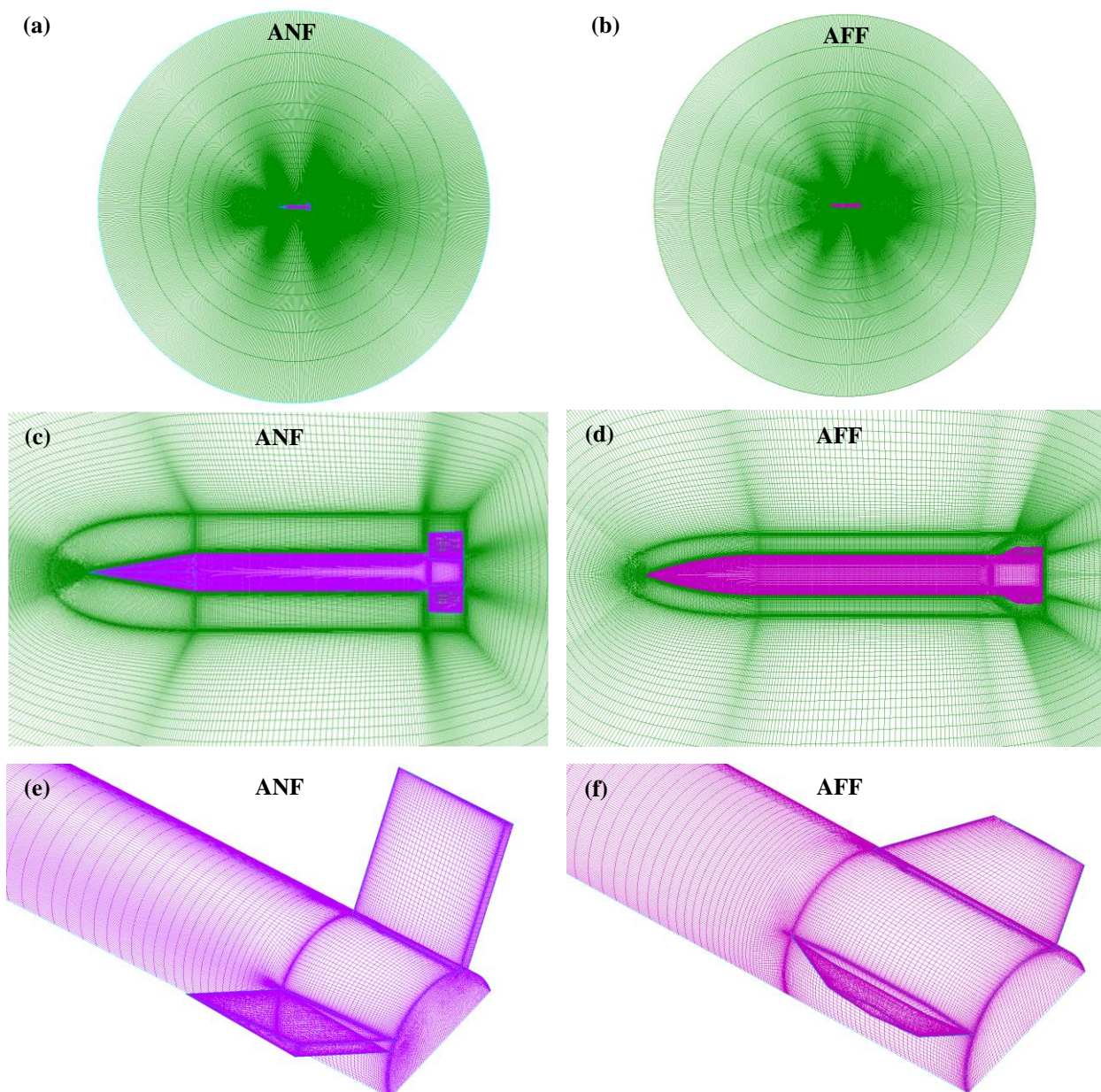|	ANF	AFF
M	2.49	2.49
Re_d	1.86×10^5	2.57×10^5
P_0	44816 Pa	61363 Pa
T_0	311.1 K	311.1 K

B. Computational Domains and Boundary Conditions

The computational domains for the ANF and AFF consisted of 14.6M and 10.8M structured hexahedral cells, respectively, (see Figure 3) generated by Pointwise V16.03R4[26] and exported in double precision format. The grids were extended ~60 calibers in the radial direction to form spherical farfield boundaries, where a characteristics-based inflow/outflow boundary condition was applied. The first cell layer from the farfield boundaries was set as an absorbing layer, where a damping source term was added in CFD++ to prevent possible numerical wave reflections which may contaminate the flow solution. The projectile walls were designated viscous adiabatic walls and utilized a solve-to-the-wall strategy where the initial grid spacing normal to the walls was 0.01 mm, satisfying the $y^+ \leq 1$ criteria for adequate boundary layer resolution.

For the ANF projectile, two grid levels were tested to demonstrate grid independence. The 14.6M-cell grid was labeled as the 'coarse' grid. This was the baseline grid. The 'fine' grid was obtained by increasing the number of grid points in each i, j, k direction by a factor of $\sim\sqrt[3]{2}$ resulting in a 30.2M-cell grid (about double the size of the coarse grid). The initial grid spacing normal to the wall was reduced to 0.0075 mm. Only a single grid level was used for the AFF.

The ANF coarse grid and the AFF grid were decomposed to run on 64 parallel processors, while the ANF fine grid was decomposed to run on 144 parallel processors. The computations were split between two supercomputers facilitated by the DoD Supercomputing Resource Center (DSRC), viz,

(i) Harold – SGI Altix ICE 8200, 1344 compute nodes, 2 quad-core Intel Xeon Nehalems and 24 GB memory per node, 4X DDR Infiniband interconnect; housed and managed by the U.S. Army Research Laboratory (ARL) DSRC at Aberdeen Proving Ground, Maryland.

(ii) Raptor – Cray XE6, 2732 compute nodes, two 8-core 2.4-GHz AMD Opterons and 32 GB memory per node, Cray Gemini interconnect; housed and managed by the U.S. Air Force Research Laboratory (AFRL) DSRC at Wright-Patterson Air Force Base, Ohio.

5

American Institute of Aeronautics and Astronautics

(a) **ANF**

(b) **AFF**

(c) **ANF**

(d) **AFF**

(e) **ANF**

(f) **AFF**

Figure 3. Computational grids for ANF (left) and AFF (right): (a–b) whole grid on symmetry plane, (c–d) nearfield grid on symmetry plane and on projectile surface, and (e–f) grid detail between fins.

C. Numerics

At prescribed flight condition, CFD++,[27] by Metacomp Technologies Inc., was used to solve the three-dimensional, compressible Reynolds-Averaged Navier-Stokes (RANS) equations in order to compute the resulting aerodynamic forces and moments acting on the projectile. Double precision format was used for all computations. First a steady-state flow solution was obtained where the projectile remained static at a prescribed angle of attack, α, relative to the freestream velocity vector. This flow solution was then used as the initial condition for the time-accurate dynamic simulation, where the projectile remained at the same angle of attack, α, while it was made to roll about its body-fixed x-axis with a constant angular velocity or spin rate, p.

1. For the steady-state static simulations:

The flow solution was advanced towards steady-state convergence using a point-implicit time integration scheme with local time-stepping, defined by the Courant-Friedrichs-Lewy (CFL) number. A linear ramping schedule was

American Institute of Aeronautics and Astronautics

used to gradually increase the CFL from 1 to 40 over the first 100 iterations, after which the CFL remained constant until convergence. The multigrid W-cycle method with a maximum of 4 cycles and a maximum of 20 coarse grid levels was used to accelerate convergence. Implicit temporal smoothing was applied for increased stability.

The spatial discretization function was a 2nd-order, upwind scheme using a Harten-Lax-van Leer-Contact (HLLC) Riemann solver utilizing Metacomp's multi-dimensional Total-Variation-Diminishing (TVD) flux limiter. First-order discretization was used for the first 200 iterations, after which blending to 2nd-order occurred over the next 100 cycles, and remained fully 2nd-order thereafter.

The turbulence model employed was Metacomp's realizable k-ε model[27,28] which solves transport equations in conservative form for the turbulent kinetic energy (k) and turbulent dissipation rate (ε). The freestream turbulence intensity was set at 2% and the turbulent-to-laminar viscosity ratio at 50. Metacomp's wall-bounded compressibility correction was applied to realize diffusive mixing in the turbulent regions which would otherwise be underpredicted in compressible flows.

Five or more orders of magnitude reduction of the cell-averaged residuals of the RANS equations was achieved within 1000-1500 iterations depending on angle of attack. However, the total aerodynamic coefficients converged relatively faster, usually within a few hundred iterations.

2. For the time-accurate dynamic simulations:

The dual-time step method was employed with the point-implicit time integration scheme utilizing a physical timestep and an inner timestep. The physical/global timestep was calculated via Eq. (9) using N=1440 iterations per rotation, which corresponds to rolling the projectile 0.25° every timestep. The inner timestep is a local non-physical timestep used to converge the RANS equations at each global/physical timestep. For the inner iterations, the multigrid W-cycle method and implicit temporal smoothing was applied. i=20 inner iterations and N=1440 iterations per rotation usually resulted in about a one order of magnitude reduction in the cell-averaged 'inner residuals' of the RANS equations, and a quasi-steady cyclical convergence of the forces and moments well within the first quarter rotation. Since the computations were very resource intensive, only one rotation was necessary, the last half of which was used to average the force and moment coefficients. The turbulence modeling used for the dynamic simulations was the same as that used for the steady-state simulations.

IV. Results

The following sections present numerically predicted total (C_X, C_N, C_m, C_{l_t}, C_Y and C_n) and dynamic derivative (C_{l_p}, C_{Y_p} and C_{n_p}) coefficients for the ANF and AFF projectiles at Mach 2.49. For the ANF, additional results are presented showing the dependence of the dynamic derivatives on spin rate, roll angle, grid resolution and integration timesteps. All plotted experimental data were obtained my digitizing data points from the plots in Reference 1, since tabulated data was not available. Baseline numerical attributes for all numerical simulations are listed in Table 2.

Table 2. Baseline Numerical Attributes

| Parameter	ANF	AFF
non-dimensional spin rate, Ω	0.015	0.030
spin rate, p	385.8 rad/s	771.6 rad/s
spin frequency, f	61.4 Hz	122.8 Hz
iterations per rotation, N	1440	1440
physical timestep, Δt	1.131×10^{-5} s	5.655×10^{-6} s
inner timesteps, i	20	20
grid size	14.6M ('coarse' grid)	10.8M (only grid level)

A. Army-Navy Basic Finner (ANF)

Figure 4 compares total aerodynamic coefficients between CFD and experiment across the angle of attack range. In the experiment, although the dynamic derivatives were computed using curve fits across multiple spin rates, total coefficient data was available at only a single spin rate of $p \approx 100$ rad/s or $p' = \Omega \approx 0.004$. The only exception was total roll moment (C_{l_t}), for which data was available at a spin rate of Ω=0.015.

The left plots in Figure 4 show total axial force (C_X), normal force (C_N) and pitching moment (C_m). CFD predictions are shown for three spin rates of Ω=0.004, 0.015 (baseline) and 0.025. The CFD results show that C_X, C_N and C_m do not vary with spin rate – a physically expected result. C_X was predicted to be higher than that of

experiment, reaching ~30% difference at α=80°. Excellent agreement between CFD and experiment was obtained for C_N and C_m at all angles of attack.

The right plots in Figure 4 show total roll moment (C_{l_t}), side force (C_Y) and yaw moment (C_n). CFD predictions are shown for two spin rates of Ω=0.015 and 0.025. The CFD results show that C_{l_t}, C_Y and C_n are spin dependent, generally increasing in magnitude at the higher spin rate. For C_{l_t}, CFD and experiment show excellent agreement at all angles of attack for Ω=0.015. For C_Y and C_n, experimental data at Ω=0.004 could not be digitized from the plots in Reference 1, due to the small magnitude of these coefficients and the large scales used for plotting. However, according to Jenke,[1] the experimental values of C_Y and C_n are very small for a spin rate of Ω=0.004 and are representative of values occurring at Ω=0. Generally, C_Y and C_n increase in magnitude at lower angles of attack, peak at α=40–60°, then decrease in magnitude.
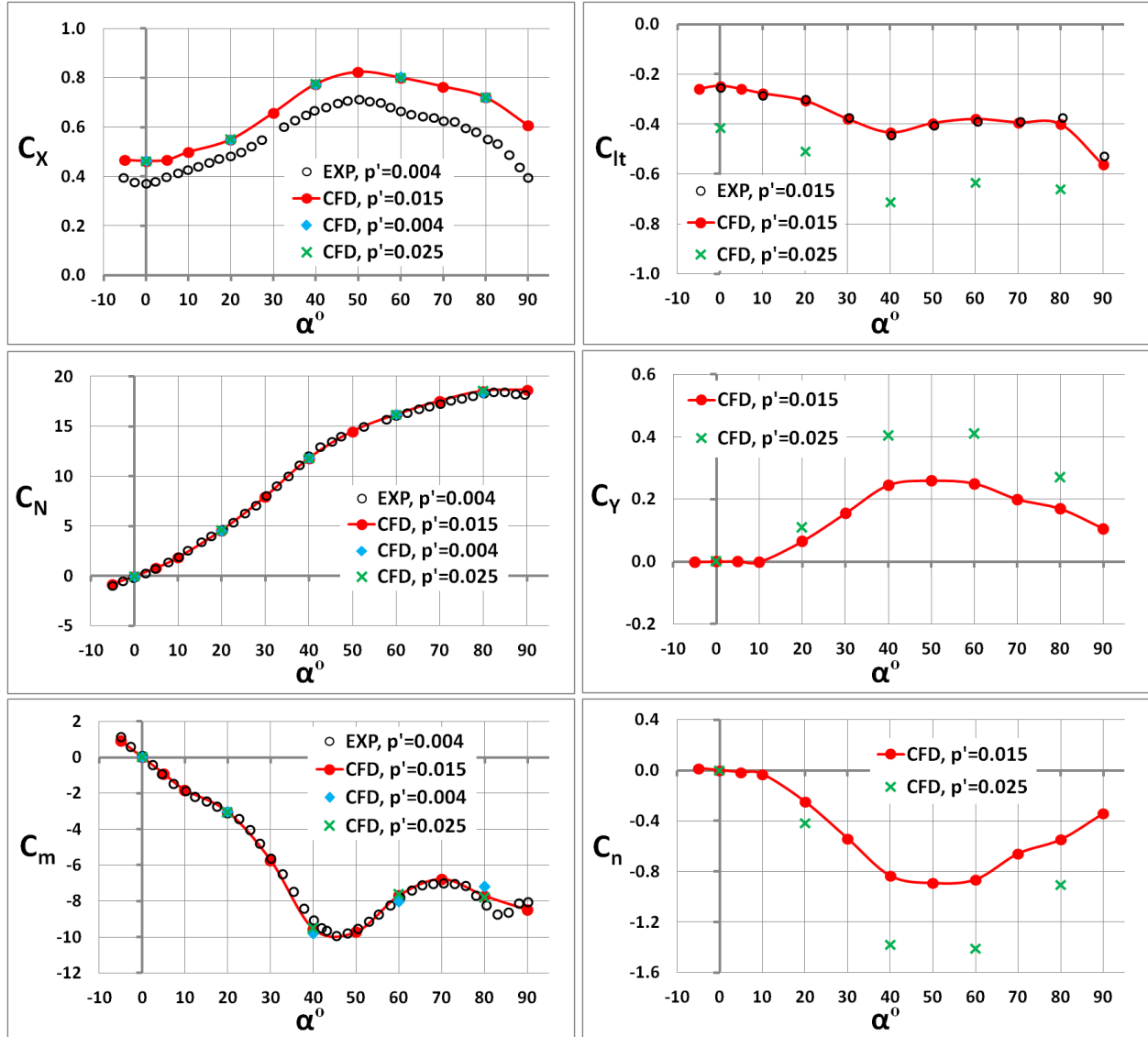

Figure 4. Total aerodynamic coefficients as a function of aoa for the ANF. For the experimental data: p≈100 rad/s or $p'=\Omega$≈0.004 for C_X, C_N, C_m; $p'=\Omega$=0.015 for C_{l_t}; and no data could be obtained for C_Y and C_n. CFD results are shown for various spin rates of $p'=\Omega$=0.004, 0.015, 0.025.

Figure 5 shows the variation of C_{l_t}, C_Y and C_n with roll angle, $\emptyset$, during a full rotation of the model for α=0, 20, 40, 60 and 80° and for Ω=0.015. Initial numerical transients mitigate within the first quarter rotation, after which the variations show quasi-steady cyclical histories. The variations generally exhibit four peaks and four troughs within

one rotation resulting from the presence of the four fins on the projectile. While the peak values of C_{l_t} increases with angle of attack, it is observed that peak values of C_Y and C_n are attained at midrange angles of attack between 40–60°, consistent with the results shown in Figure 4. Given the observed quasi-steady convergence of the total coefficients, only one rotation was necessary for the computations. The total coefficients were therefore computed as averages over the last half rotation of the projectile. It was these averages that were plotted in Figure 4, and were used to calculate the dynamic coefficients depicted in Figure 7.
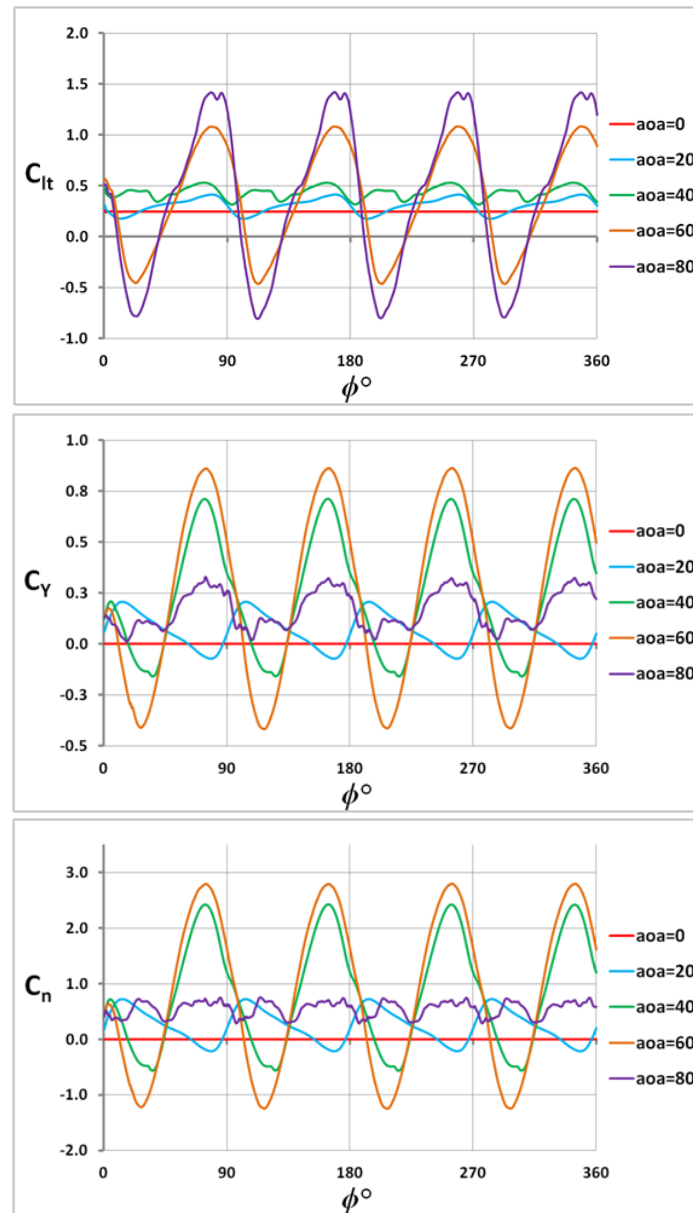
Figure 5. Variation of CFD total coefficients with roll angle, $\emptyset$, for the ANF. Ω=0.015.

The dynamic coefficients were computed in the experiment as 'spin derivatives' and were defined by Eqs. (4)–(6). Prior to computing the dynamic coefficients, therefore, the behavior of the total coefficients with spin rate was investigated for α=0, 20, 40, 60 and 80° using two spin rates of Ω=0.015 and 0.025. Figure 6 plots C_{l_t}, C_Y and C_n as a function of spin rate. The line plots are least-squares linear regression fits to the CFD data. Since C_{l_t}, C_Y and C_n are expected to be zero for Ω=0, then the linear fits were forced to intercept the origin. Since all of the linear fits have a

American Institute of Aeronautics and Astronautics

correlation coefficient of $R^2 \approx 1$ (accurate to at least 3 decimal places), then it is assumed that C_{l_t}, C_Y and C_n vary linearly with spin rate, allowing simple implementaion of Eqs. (4)–(6) to calculate the dynamic spin derivatives.
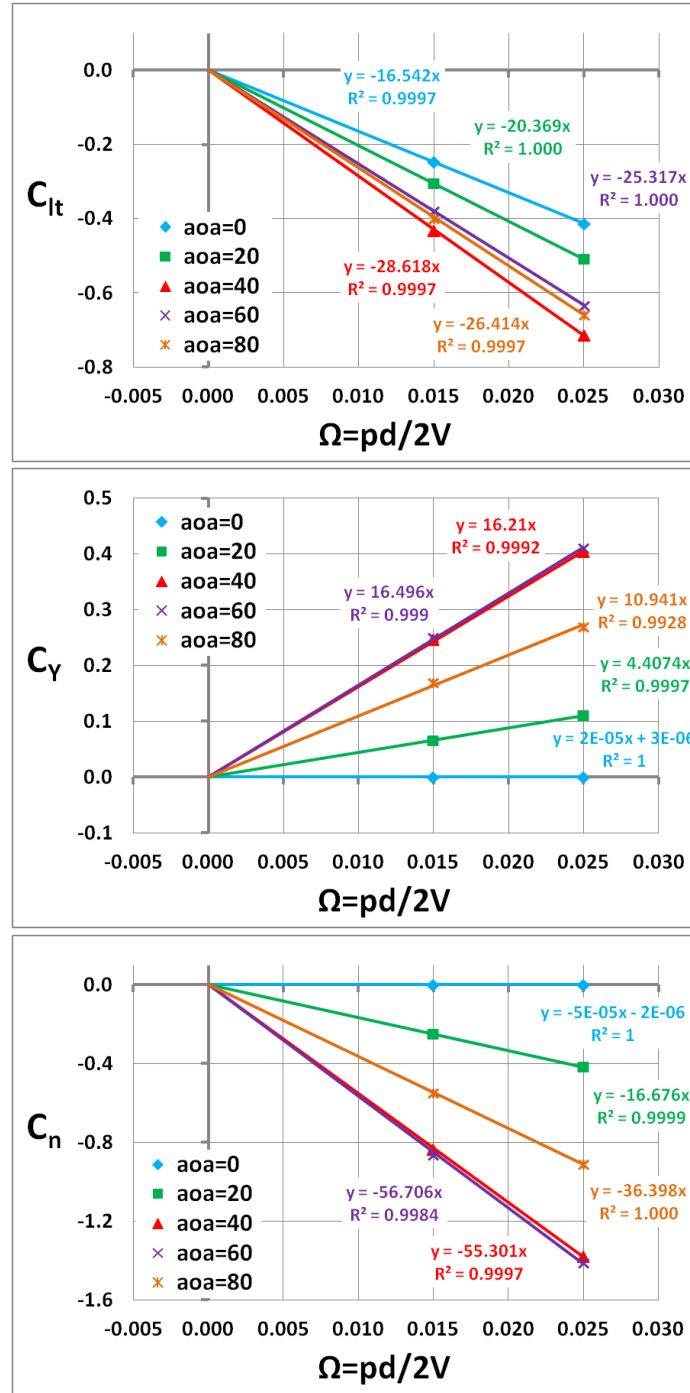
Figure 6. CFD total coefficients as a function of spin rate for the ANF. Ω=0.015 and 0.025.

Figure 7 shows the computed dynamic derivatives, viz, roll damping moment (C_{l_p}), Magnus force spin derivative (C_{Y_p}) and Magnus moment spin derivative (C_{n_p}), as a function of angle of attack. As previously stated, the experimental dynamic derivatives were computed by curve fitting data across multiple spin rates. CFD results are shown for two spin rates of Ω=0.015 and 0.025. There are no observable differences in the CFD results between

10

American Institute of Aeronautics and Astronautics

Ω=0.015 and 0.025 for all three dynamic derivatives (an expected result based on the linearity conclusions from Figure 6). The C_{l_p} CFD results show excellent agreement with experiment, showing moderate increases in magnitude as angle of attack increases. For C_{Y_p} and C_{n_p}, the CFD results compare very well with experiment up to 30°, after which C_{Y_p} is under-predicted, and C_{n_p} is over-predicted for the remainder of the α–range. The differences reach ~20% at α=50° for both C_{Y_p} and C_{n_p}. C_{Y_p} and C_{n_p} show significant increases in magnitude as angle of attack increases, peaking at α=40–60°, similar to the trends observed for corresponding C_Y and C_n total coefficients.
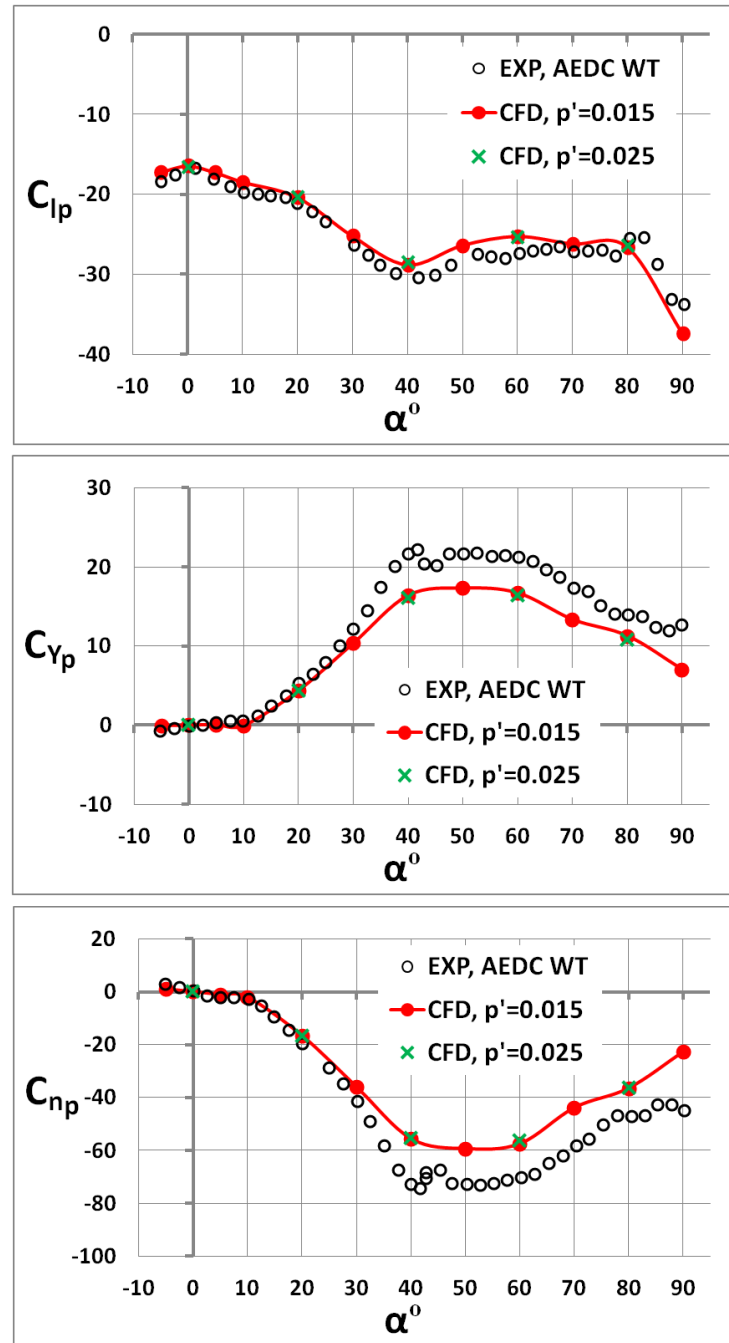
Figure 7. Dynamic coefficients, viz, roll damping moment (C_{l_p}), Magnus force spin derivative (C_{Y_p}) and Magnus moment spin derivative (C_{n_p}), as a function of aoa for the ANF.

Dependence of the results on numerical modeling parameters were investigated for the ANF. Except for the numerical parameter being investigated, baseline settings were used for all simulations. Table 3 shows the dependence of the dynamic coefficients on grid resolution. As previously stated, two grid levels were used, viz, the 'coarse' grid (baseline grid, 14.6M cells) and the 'fine' grid (30.2M cells). Results were obtained at α=0, 20, 40, 60 and 80°. Except perhaps at α=80°, the percent differences depicted in Table 3 are small enough to deem the coarse grid sufficient for accurately computing the dynamic coefficients. The percent differences at α=80° are still reasonable and are within experimental error margins, reaching 2.3%, 4.7% and 0.8% for C_{l_p}, C_{Y_p} and C_{n_p}, respectively.

Table 3. Dependence of Dynamic Coefficients on Grid Resolution. Coarse=14.6M Cells. Fine=30.2M Cells

$\alpha°$	C_{l_p}			C_{Y_p}			C_{n_p}			CPU sec/iter	
	Coarse	Fine	Diff	Coarse	Fine	Diff	Coarse	Fine	Diff	Coarse	Fine
0	-16.43	-16.43	0.0%	0.00	0.00	0.0%	0.00	0.00	0.0%	67	71
20	-20.37	-20.44	-0.4%	4.38	4.35	0.7%	-16.62	-16.59	0.2%	53	60
40	-28.82	-28.91	-0.3%	16.39	16.76	-2.3%	-55.66	-56.63	-1.7%	54	84
60	-25.25	-25.24	0.0%	16.70	17.01	-1.9%	-57.58	-57.75	-0.3%	53	-
80	-26.61	-27.22	-2.3%	11.29	11.82	-4.7%	-36.50	-36.19	0.8%	96	-

Table 4 shows the dependence of the dynamic coefficients on the physical timestep used for numerically advancing the solution in time. The physical timestep was calculated via Eq. (9) based on a chosen number of iterations per rotation, N. The physical timestep was varied using N=720, 1440, 2880, corresponding to rolling the projectile 0.5°, 0.25° and 0.125°, respectively, every timestep. Table 4 shows small differences in the dynamic coefficients between N=720 and N=1440, and even smaller negligible differences between N=1440 and N=2880. Previously, N=360 and N=720 were typical choices at low angles of attack and for supersonic Mach numbers, as suggested by some studies.[14] However, at higher angles of attack, N=1440 resulted in better numerical stability, better convergence of the 'inner' residuals of the RANS equations, and smoother quasi-steady histories of the total coefficients. Therefore, N=1440 was used as the baseline number of timesteps per rotation for the simulations.

Table 4. Dependence of Dynamic Coefficients on Physical Timestep

$\alpha°$	C_{l_p}			C_{Y_p}			C_{n_p}			CPU sec/iter		
	N=720	N=1440	N=2880	N=720	N=1440	N=2880	N=720	N=1440	N=2880	N=720	N=1440	N=2880
0	-16.44	-16.43	-16.43	0.00	0.00	0.00	0.00	0.00	0.00	68	67	68
40	-28.95	-28.82	-28.78	16.87	16.39	16.31	-56.07	-55.66	-55.72	67	54	46
80	-27.89	-26.61	-26.13	12.89	11.29	10.96	-36.78	-36.50	-36.90	154	96	66

Table 5 shows the dependence of the dynamic coefficients on the number of inner iterations, i. Inner iterations are used to converge the RANS equations at each physical timestep. Typically i=10–20 was deemed sufficient at low angles of attack, as suggested by previous studies.[14] For higher angles of attack, it was observed that i=20 provided more stable numerics and better convergence of the inner RANS residuals. Table 5 shows no significant change in results between i=20 and 40, indicating that the i=20 baseline value was sufficient for the computations.

Table 5. Dependence of Dynamic Coefficients on the Number of Inner Iterations

$\alpha°$	C_{l_p}		C_{Y_p}		C_{n_p}		CPU sec/iter	
	i=20	i=40	i=20	i=40	i=20	i=40	i=20	i=40
0	-16.43	-16.43	0.00	0.00	0.00	0.00	67	67
40	-28.82	-28.82	16.39	16.39	-55.66	-55.66	54	67
80	-26.61	-26.61	11.29	11.28	-36.50	-36.49	96	101

The dependence of the results on other numerical parameters was tested. Changing these parameters affected the stability of the numerical computations and, in some cases, provided much better results for the total and dynamic coefficients at high angles of attack. These parameters included: (i) using a node-based Total Variation Diminishing (TVD) polynomial scheme instead of a centroidal-based one; CFD++ uses TVD polynomial interpolation to limit spurious oscillations of fluxes across grid cells, particularly where solution discontinuities exist, (ii) using a 'hypersonic pressure switch' in CFD++, which aggressively applies pressure dissipation in regions where the pressure variations are greater than a specified threshold level, and (iii) decreasing the implicit temporal smoothing factor from its default value of 0.75 to 0.5, although this produced only slight differences in the results; temporal smoothing helps to overcome strong initial transients and helps to increase the stable operating CFL number for improved convergence.

B. Air Force Modified Basic Finner (AFF)

The total and dynamic coefficients were computed for the AFF projectile using the baseline numerical settings stated in Table 2. Other than geometry, the major difference between the ANF and AFF simulations was that the non-dimensional spin rate used for the latter was $\Omega=0.030$, as opposed to $\Omega=0.015$ for the former. No numerical parameter studies were conducted for this projectile. Figure 8 compares total aerodynamic coefficients between CFD and experiment across the angle of attack range. Like the ANF, in the experiment, although the dynamic derivatives were computed using curve fits across multiple spin rates, total coefficient data was available at only a single spin rate of $p\approx100$ rad/s or $p'=\Omega\approx0.004$. The only exception was total roll moment (C_{l_t}), for which data was available at a spin rate of $\Omega=0.030$.

C_X, C_N and C_m (left plots in Figure 8) are, in this case, theoretically independent of spin rate. C_X shows agreement with experiment up to $\alpha=10°$, after which CFD predicts C_X to be higher than experiment, almost doubling that of the experiment at the higher angles of attack. C_N and C_m show excellent agreement with experiment, and show significant increases in magnitude as angle of attack increases.

Spin dependent coefficients, viz, C_{l_t}, C_Y and C_n, are shown on the right in Figure 8. C_{l_t} shows excellent agreement with experiment up to $\alpha\approx70°$, after which there is a ~16% discrepancy at $\alpha=80°$ and 90°. For C_Y and C_n, experimental data at $\Omega=0.004$ could not be digitized from the plots in Reference 1, due to the small magnitude of these coefficients and the large scales used for plotting. However, according to Jenke,[1] the experimental values of C_Y and C_n are very small for a spin rate of $\Omega=0.004$ and are representative of values occurring at $\Omega=0$. Therefore, only CFD results for $\Omega=0.030$ are shown for C_Y and C_n. Generally, C_Y and C_n initially increase in magnitude and peak at $\alpha\approx50°$.

Figure 9 shows the computed dynamic derivatives, viz, roll damping moment (C_{l_p}), Magnus force spin derivative (C_{Y_p}) and Magnus moment spin derivative (C_{n_p}), as a function of angle of attack. The CFD results show excellent agreement with experiment for $\alpha=0$–40°, after which there is only slight discrepancy with experiment up to $\alpha=90°$. The magnitudes of all three coefficients show significant increases, particularly for the Magnus moment, as angle of attack increases.
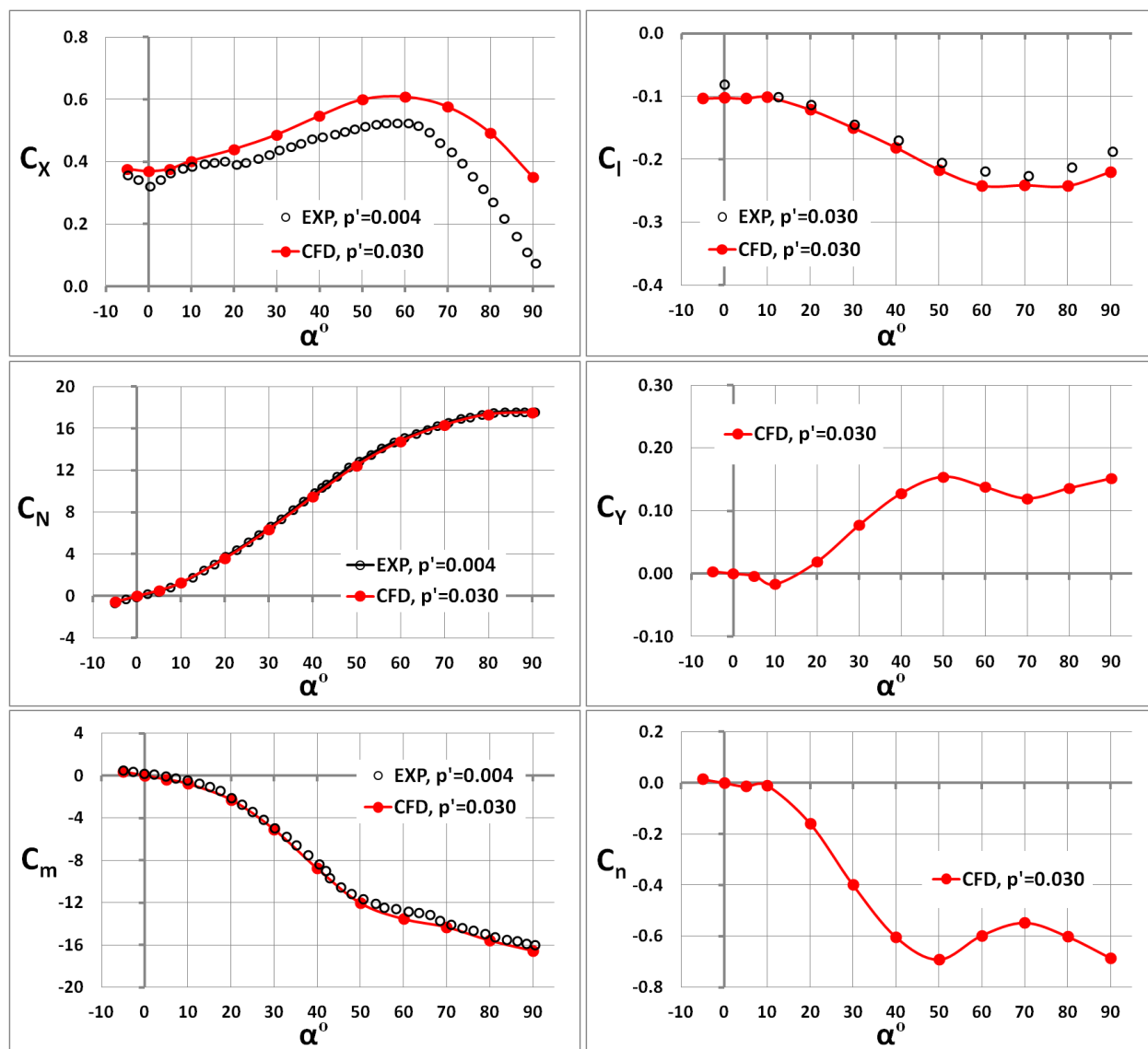
Figure 8. Total aerodynamic coefficients as a function of aoa for the AFF. For the experimental data: $p \approx 100$ rad/s or $p' = \Omega \approx 0.004$ for C_X, C_N, C_m; $p' = \Omega = 0.030$ for C_{l_t}; and no data could be obtained for C_Y and C_n. CFD results are shown for a single spin rate of $p' = \Omega = 0.030$.
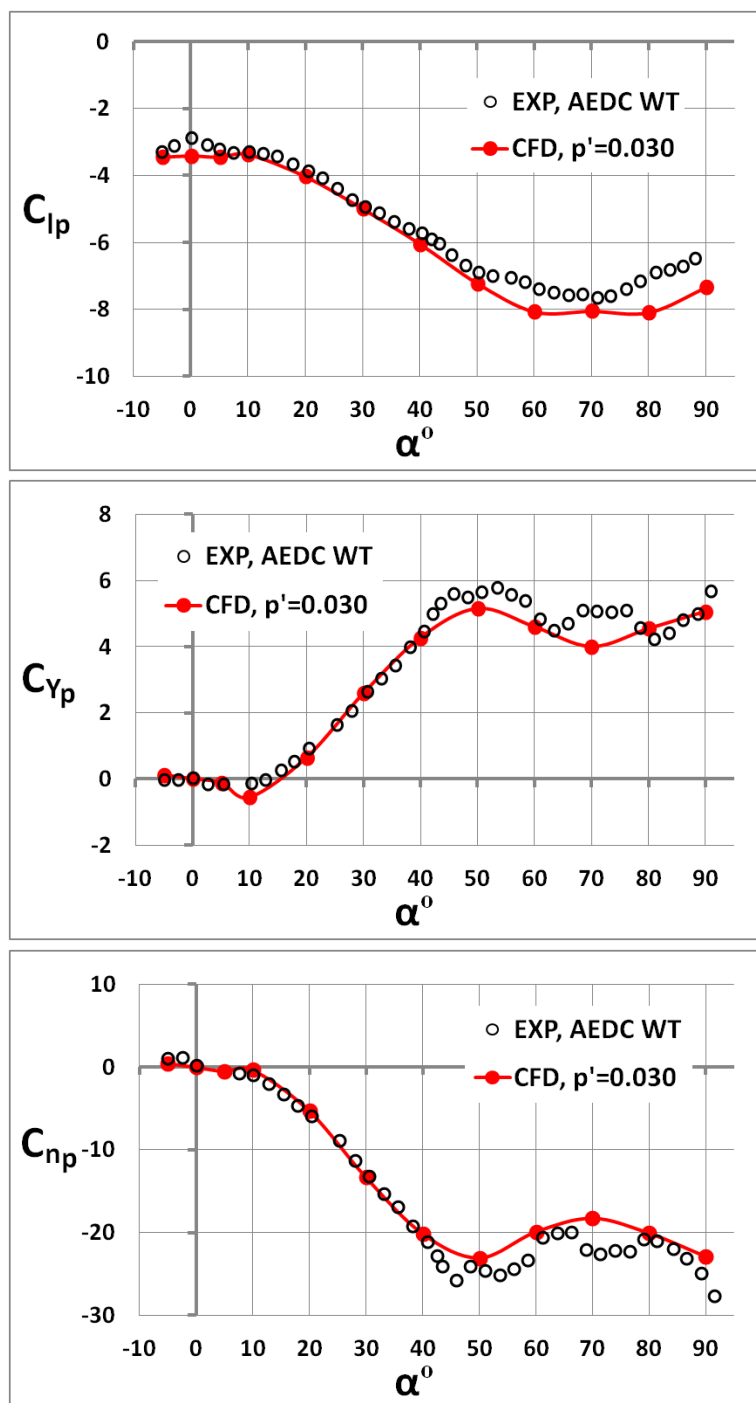
Figure 9. Dynamic coefficients, viz, roll damping moment (C_{l_p}), Magnus force spin derivative (C_{Y_p}) and Magnus moment spin derivative (C_{n_p}), as a function of aoa for the AFF.

V. Conclusion

The total and dynamic derivative aerodynamic coefficients were computed at Mach 2.49 for angles of attack ranging from -5–90° for two fin-stabilized reference projectiles, viz, the Army-Navy Basic Finner and the Air Force Modified Basic Finner. Time-accurate Reynolds-averaged Navier-Stokes numerical methods were used to obtain the aerodynamic forces and moments acting on the projectiles as they underwent a simulated axial roll at constant angular velocity. Archival wind tunnel data from Arnold Engineering and Development Center at Arnold Air Force Base, Tennessee was used to validate the CFD results.

Total coefficients: For both projectiles, the axial force was generally over-predicted, while the normal force, pitching moment and roll moment showed excellent agreement with experiment for the full angle of attack range. The predicted side force and yaw moment could not be compared with experiment due to a lack of data. The quasi-steady cyclical behavior of the total coefficients was demonstrated, requiring these coefficients to be averaged over a chosen number of cycles. The linear variation of the total coefficients with spin rate was demonstrated – a proportionality assumption that allows the dynamic coefficients to be calculated via the methods used herein.

Dynamic coefficients: For both projectiles, the roll damping moment, Magnus force and Magnus moment showed excellent agreement with experiment up to about 30–40° angle of attack, after which the comparisons showed only little discrepancy. Using two grid sizes, the results were shown to be independent of the baseline grid resolution used in this study. The numerical stability and accuracy of the results can be very dependent on the spatial and temporal integration parameters at high angles of attack. This is due to the more complex physical aerodynamic interactions occurring at these high angles of attack, such as unsteady vortex-body interactions, shock-fin interactions and unsteady low-speed wake flows. Numerical parameters investigated in this study were physical integration timestep, non-physical inner timestep, localized pressure dissipation switches, nodal versus centroidal based polynomial flux limiters and temporal smoothing. Although numerical settings were recommended in this study, these may vary with projectile geometry, Mach number and other flight conditions.

This study successfully demonstrated the capability of time-accurate Reynolds-averaged Navier Stokes numerical methods to compute dynamic stability derivatives for finned projectiles flying supersonically at high angles of attack up to 90°. Further investigations may include subsonic and transonic Mach number regimes, varying Reynolds numbers, the effect of fin cant, and more detailed investigations of the physical aerodynamic interactions at high angles of attack.

VI. Acknowledgments

VII. References

[1]Jenke, L M, "Experimental Roll-Damping, Magnus, and Static-Stability Characteristics of Two Slender Missile Configurations at High Angles of Attack (0–90 deg) and Mach Numbers 0.2 through 2.5," Arnold Engineering and Development Center, AEDC-TR-76-58, Jul 1976

[2]Dupuis, A D, Hathaway, W, "Aeroballistic Range Tests of the Basic Finner Reference Projectile at Supersonic Velocities," DREV-TM-9703, Defense Research Establishment, Valcartier, Canada, Aug 1997

[3]Dupuis, A, "Aeroballistic Range and Wind Tunnel Tests of the Basic Finner Reference Projectile from Subsonic to High Supersonic Velocities," TM 2002-136, Defense R&D Canada Valcartier, Oct 2002

[4]Dupuis, A D, Hathaway, W, "Aeroballistic Range Tests of the Air Force Finner Reference Projectile," TM 2002-008, Defense R&D Canada Valcartier, May 2002

[5]West, K O, "Comparison of Free Flight Spark Range and Wind Tunnel Test Data for a Generic Missile Configuration at Mach Numbers From 0.6 to 2.5," Air Force Armament Laboratory, Eglin Air Force Base, FL, AFATL-TR-81-87, Oct 1981

[6]West, K O, Whyte, R H, "Free Flight and Wind Tunnel Test of a Missile Configuration at Subsonic and Transonic Mach Numbers with Angles of Attack up to 30 Degrees," 11th Navy Aeroballistic Symposium, Warminster, PA, Aug 1978

[7]Bhagwandin, V A, Sahu, J, "Numerical Prediction of Pitch Damping Stability Derivatives for Finned Projectiles," AIAA-2011-3028, June 2011

[8]DeSpirito, J, Heavey, K R, "CFD Computation of Magnus Moment and Roll Damping Moment of a Spinning Projectile," AIAA 2004-4713, Aug 2004

[9]DeSpirito, J, Silton, S I, Weinacht, P, "Navier-Stokes Predictions of Dynamic Stability Derivatives: Evaluation of Steady-State Methods," AIAA 2008-214, Jan 2008

[10] Murman, S M, "Reduced-Frequency Approach for Calculating Dynamic Derivatives," AIAA Journal, Vol 45, No 6, June 2007

[11] Oktay, E, Akay, H, "CFD Predictions Of Dynamic Derivatives for Missiles," AIAA 2002-0276, Jan 2002

[12] Park, S H, Kim, Y, Kwon, J H, "Prediction of Damping Coefficients Using the Unsteady Euler Equations," AIAA Journal of Spacecraft and Rockets, Vol 40, No 3, May-June 2003

[13] Park, S H, Kwon, J H, Kim, Y, "Prediction of Dynamic Damping Coefficients Using Unsteady Dual-Time Stepping Method," AIAA 2002-0715, Jan 2002

[14] Sahu, J, "Numerical Computations of Dynamic Derivatives of a Finned Projectile Using a Time-Accurate CFD Method," AIAA 2007-6581

[15] Schiff, L B, "Non-linear Aerodynamics of Bodies in Coning Motion," AIAA Journal, Vol 10, No 11, pp 1517-1522, Nov 1972

[16] Schiff, L B, Tobak, M, "Results from a New Wind Tunnel Apparatus for Studying Coning Motions of Bodies of Revolution," AIAA Journal, Vol 8, No 11, pp 1953-1957, Nov 1970

[17] Stalnaker, J F, Robinson, M A, "Computation of Stability Derivatives of Spinning Missiles Using Unstructured Cartesian Meshes," AIAA 2002-2802, Jun 2002

[18] Tobak, M, Schiff, L B, "Generalized Formulation of Nonlinear Pitch-Yaw-Roll Coupling: Part I—Nonaxisymmetric Bodies," AIAA Journal, Vol. 13, No. 3, pp. 323–326, March 1975

[19] Tobak, M, Schiff, L B, "Generalized Formulation of Nonlinear Pitch-Yaw-Roll Coupling: Part II—Nonlinear Coning Rate," AIAA Journal, Vol. 13, No. 3, pp. 327–332, March 1975

[20] Weinacht, P, "Characterization of Small-Caliber Ammunition Performance Using a Virtual Wind Tunnel Approach," AIAA 2007-6579, Aug 2007

[21] Weinacht, P, "Projectile Performance, Stability, and Free-Flight Motion Prediction Using Computational Fluid Dynamics," AIAA Journal of Spacecraft and Rockets, Vol 41, No 2, Mar-Apr 2004

[22] Weinacht, P, Sturek, W B, "Computation of the Roll Characteristics of a Finned Projectile," AIAA Journal of Spacecraft and Rockets, Vol 33, No 6, Nov-Dec 1996

[23] Carlucci, D E, Jacobson, S S, "Ballistics: Theory and Design of Guns and Ammunition," CRC Press, Taylor and Francis Group, LLC, Boca Raton, FL, 2008

[24] McCoy, R L, "Modern Exterior Ballistics," Schiffer Publishing Ltd, Atglen, PA, 1999

[25] Murphy, C H, "Free Flight Motion of Symmetric Missiles," U.S. Army Research Laboratory, Aberdeen Proving Ground, MD, BRL 1216, July 1963

[26] Pointwise, Inc., "Pointwise User Manual," Fort Worth, TX, 2010

[27] Metacomp Technologies, Inc., "CFD++ User Manual," Agoura Hills, CA, 2007

[28] Chien, K-Y, "Predictions of Channel and Boundary Layer Flows with a Low-Reynolds-Number Turbulence Model," AIAA Journal, Vol 20, No 1, 1982